# Vector-Field-Based Deformable Models for Radiation Dosimetry

Rongxin Li[1], Donald McLean[2] and Sébastien Ourselin[1]

[1]BioMedIA Lab, CSIRO ICT Centre and [2]Westmead Hospital, Sydney.

## Abstract

*Accurate age-specific models of pediatric patients for radiation dosimetry purposes are not presently available. In a world-first effort to build such models, we are currently developing a scheme that combines deformable models with a priori anatomical knowledge and minimal human supervision. However, the outcome of applying a deformable model is often significantly dependent on its initialization. This is an obstacle to accurate and robust automatic or near-automatic segmentation. In this paper, we propose a novel approach to reducing this sensitivity to initialization by deriving a vector field from topographic and Euclidean distance transforms. It is aimed to extend the influence of target gradients over the entire image in a consistent fashion, while enabling the model to ignore irrelevant gradients. Initiated by one or more seeds, the vector field is computed using an efficient numerical method, and has so far been integrated into a parametric (snake) model and a geodesic active contour level set model. Preliminary experiments targeting different organs have shown that this is a highly promising approach. We believe that this approach will satisfy the need for a high degree of automation in using deformable models for our dosimetry work.*

## 1 Introduction

Radiation exposure from diagnostic procedures increases the risk of cancer development later in life, particularly when large radiation doses are involved. This is especially relevant for pediatric patients. Accurate estimation of the amount of radiation energy deposited in various tissues within the body resulting from a radiological procedure constitutes an essential scientific basis for the determination of the optimal dose. Numerical simulation via a Monte Carlo radiation transport code has proven to be effective for this purpose. However, the simulation requires a computational model as a "virtual phantom" that represents the typical patient. Unfortunately, no accurate models for children currently exist. Scaled-down adult models are not sufficiently accurate as they do not take into account the proportional differences between adults and children. In a

world-first effort to build precise pediatric models, we aim to establish a large and dynamically growing database of CT and MR images of pediatric patients, and to construct the models on this basis. This model building requires that the data be first segmented into different tissues, however it is not feasible to delineate each organ via manual methods. We are currently developing a scheme that combines the deformable model approach with *a priori* anatomical knowledge and minimal human supervision. However, the outcome of applying a deformable model is often significantly dependent on its initialization, mainly because the model generally has a tendency to converge upon encountering the first set of significant gradients on its path of evolution. This is an obstacle to accurate and robust automatic or near-automatic segmentation. In this paper, we present the first stage of our radiation dosimetry work. This is a novel approach aimed at reducing the models' dependence on initialization and parameters in order to achieve a higher degree of automation.

## 2 Related Work

The earliest deformable model [3] had very limited capture ranges. Early attempts to improve this include a balloon model which applies either a constant or a gradient-adaptive force in the direction of the contour or surface normal. The geodesic active contour (GAC) model [1] introduced later incorporates propagation and advection terms. Although these measures help relax initialization requirements, they do not completely remove the need for the initialization to meet certain conditions [13]. Another widely applied approach is to modify the external force. The gradient vector flow (GVF) method [16, 13] is perhaps the most prominent example, which uses a spatial diffusion of the gradient of an edge map to supply an external force. This technique enables gradient forces to extend from the boundary of the object, and has an improved ability to deal with concavities over using distances from edgels [2, 16]. A major drawback of this approach, however, is that it cannot discriminate between target and irrelevant edges. A third approach is hybrid segmentation. Various other techniques (*e.g.* multiresolution processing and *ad hoc* search methods), have also been used in attempts to relax the initialization require-

ments. Although deformable models' sensitivity to initialization has attracted significant research interest and effort, a robust generic approach has not yet been available.

## 3 Influence Zones Based on Topographic Distance

We examine a metric based image partition approach [8] for the purposes stated above. Given K+1 sets of connected voxels $\{S_i : i \in I\}$ as the partition seeds, where $I = \{0, 1, 2, \ldots, K\}$, and a measure $d(x, y)$ that defines the distance in a domain $D$ between points $x \in D$ and $y \in D$, a Skeleton by Influence Zones (SKIZ, alternatively known as a generalized Voronoi Diagram) can be generated based on the corresponding distance metric. Defining the distance from $x$ to $Y \subset D$ as $d(x, Y) = \inf_{y \in Y} d'(x, y)$, the influence zone of $S_i$, for example, is

$$Z_i = \{x \in D : \forall j \in I\backslash\{i\}[d(x, S_i) < d(x, S_j)]\}$$

The distance measure used for SKIZ needs to be linked to the image intensity in order for it to be applicable to image segmentation. One such measure is the topographic distance on a gradient image. In fact, it has been established that SKIZ with respect to the geodesic topographic distance is equivalent to the watershed of the image [8, 11], and this has been used in the metric-based definition of the watershed transform [8, 14]. This is the basis of partial differential equation (PDE) models of the watershed [7, 12], which have been exploited to incorporate smoothness into the watershed segmentation [12]. The geodesic topographic distance (GTD) from a point $x$ to the $i$th seed, given a $C^2$ real function $f$ on a continuous domain $D_c$ as the relief image, is $\tau_i(x) = \inf_{\gamma \in \{\Gamma(x, y): y \in S_i\}} \int_\gamma |\nabla f(s)| ds$, where $\Gamma(x, y)$ is the set of all paths from $x$ to $y$. Suppose $S_i$ is entirely on a local minimum of $f$. Let $\delta_i(x) = f(s_i^c) + \tau_i(x)$, where $i \in I$, $s_i^c \in S_i$. Based on the GTDs, $D_c$ can be partitioned into overlapping sub-sets

$$\{\Omega_i = \{x \in D_c : \forall j \in I\backslash\{i\} \, [\delta_i(x) \leq \delta_j(x)]\}, i \in I\}. \tag{1}$$

It can be proven that $\partial\Omega_i \cap \partial\Omega_j$ coincides with the most significant gradient on a geodesic path (with respect to the topographic distance) between the two corresponding seeds [12, 8]. This is illustrated in Figure 1, where a 1D image is used for simplification. Note that the strength and the continuity of the gradients are both necessary in $n$D with $n > 1$.

A sometimes overlooked condition for the above to hold, in general, is that the seeds are at local minima of $f$, and that these are the only local minima in the image. If this condition is not satisfied (e.g. in a case such as the middle image in Figure 1), homotopy modification or swamping [9, 8] may need to be performed. so as to obtain an image like that illustrated at the bottom of Figure 1.

We exploit the relationship outlined above for the purpose of supplying an external force to a deformable model. We selectively expose the boundary gradients of the object of segmentation as the strongest continuous edge between the seeds, and combine the outcome with the Fast Marching Method [15], as discussed in the following sections.
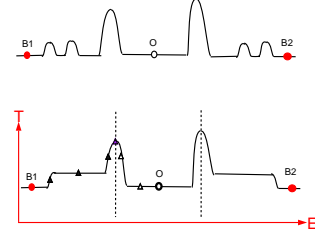


**Figure 1.** *Topographic SKIZ partitions an image along the largest gradients between the seeds. Top: A gradient magnitude image as the relief image, object marker O (open circle) and background marker B1 and B2 (red filled circles). Bottom: Modified homotopy given the seeds; in terms of the distance traveled along axis T (topographic distance), the filled triangles are closer to the marker B1, whereas the open triangles are nearer to the marker O. SKIZ positions are marked by the vertical dash lines.*

## 4 Globally Consistent Vector Field

**Dual Marking Scenario** First, we discuss the scenario that segmentation seeds (connected components) are provided to identify both the target and the background. We also call these identification markers. They consist of one placed interior to the boundary of the target organ, and one or more external to the target. More than one background marker is usually not necessary but can however result in more robustness where the image is complex. This will be demonstrated later. Without loss of generality, suppose that $S_0$ is placed within the target of segmentation, and $\{S_j : j \in \{1, 2, \ldots, K\}\}$ are placed outside in the background. We compute a maximum difference image $M$ in which

$$M(x) = \max_{j \in I}\{\delta_0(x) - \delta_j(x)\} \tag{2}$$

This operation can be implemented very efficiently, as shown in 5.2. In order for it to be applicable to parametric and Statistical deformable models, we inversely threshold $M$ to obtain a binary image $B_0(x) = \begin{cases} 1, & M(x) \leq 0 \\ 0, & \texttt{otherwise} \end{cases}$. $B_0(x)$ itself is unlikely to be an optimal segmentation of the target, due to degradation or deficiencies in the boundary

gradients that are often present, and a lack of model constraints (*e.g.* smoothness, shape constraints) to overcome these deficiencies. It is possible to use $B_0$ for the initialization of the model. This is analogous to the hybrid segmentation approach reviewed in Section 2. Special care, however, must be taken if it is possible that the target encloses significant internal gradients, due either to noise or to sub-entities with varying intensities[1]. It is sufficient, and more robust, to use a globally consistent flow field that can be integrated into a deformable model, without necessarily using the above initialization strategy. A further advantage of doing so is that some isolated gradients, while not playing a role in defining $B_0$, can be additionally taken into account. For this, we first compute a distance map $D_0$ on image $B_0$, *i.e.* $D_0 = \mathrm{E}(B_0)$, where E is a Euclidean distance transform. This information may be used similarly to a method proposed in [2], where a distance map to edgels is used. A complimentary set of computation follows, namely, $B_1(\boldsymbol{x}) = \overline{B_0(\boldsymbol{x})}$, $D_1 = \mathrm{E}(B_1)$. These will be used to compute the vector field. In order to overcome potential problems near deep concavities[16], a pressure force or propagation term that incorporates the sign of $M$, $sgn[M(\boldsymbol{x})]$, can be used. This makes the force or propagation automatically adaptive to inflation or deflation requirements, in accordance with whether the part of the model is inside or outside of the segmentation object. This is a significant advantage of our approach.

**Single Marking Alternative**  Under some circumstances it may be more desirable to use a single seed, especially in applications that use fully automatic initialization. If all internal gradients present within the target are known to be isolated (*e.g.* those due to imaging noise or artifacts), or are significantly weaker compared with those at the object boundary, the difference between the GTDs on either side of the boundary should be large enough for a segregating threshold to be easily found. In such a case, a binary image $B_0$ can be obtained by $B_0(\boldsymbol{x}) = \begin{cases} 1, & \delta_0(\boldsymbol{x}) \le \eta \\ 0, & \texttt{otherwise} \end{cases}$, where $\eta$ is an application-dependent constant. $D_0$, $B_1$ and $D_1$ can be calculated similarly to the methods presented above. However, this method cannot be used where the gradient composition interior to the target cannot be estimated *a priori*.

**Integration with Deformable Models**  For a parametric model, we obtain the following vector field

$$\mathbf{F} = \begin{cases} -m_D \nabla D, & |\nabla D'| = 0, |\nabla D| \neq 0 \\ -\nabla E, & 0 < |\nabla D'| \le h \\ -m_{D'} \nabla D', & |\nabla D'| > h \end{cases} \quad , \quad (3)$$

[1]This can be either due to the inherent anatomy of the entity of interest (*e.g.* an aortic aneurysm that surrounds a contrast enhanced blood flow channel) or because of various pathologies (*e.g.* calcifications) or artifacts (*e.g.* stent grafts).

where $E = -|\nabla(G_\sigma * I)|^2$, $h$, $m_D$ are constant parameters. Smaller $|\nabla D'|$ values are present near the ridge (or skeleton) of the object. The above conditional is designed to improve the performance on high-curvature convex parts, or very thin components of the object. $F$ has the potential to replace the gradient image with "cleaned up" vectors that are globally consistent, in contrast to the short range and inconsistent information in the gradient image. A flow field such as Eq. 3 can be readily integrated into a parametric or a geometric deformable model, as demonstrated in existing works with the GVF model [16, 13]. For example, $F$ can help drive the deformation of a parametric model $\mathbf{v}$ with a surface parameterization $s$ as follows:

$$\frac{\partial \mathbf{v}}{\partial t} = -\beta \frac{\partial^4 \mathbf{v}}{\partial s^4} + (\mathbf{F}(\mathbf{x}) \cdot \mathbf{N}(\mathbf{x}))\mathbf{N}(\mathbf{x}), \quad (4)$$

where $\mathbf{N}$ is the surface normal, $\beta$ is one of the model parameters. As $\mathbf{F}$ may be perpendicular to $\mathbf{N}$ in some situations, notably inside concavities[16], a pressure force $\gamma\mathbf{N}(\mathbf{x})$ or $\gamma\{sgn[M(\mathbf{x})]\}\mathbf{N}(\mathbf{x})$ is used to deal with these situations. The latter form represents a distinct advantage of this approach as it is adaptive, in that it is automatically either inflating or deflating according to whether the node of the model is inside or outside of the segmentation object.

Regarding a level set model [15], previous examples exist of integrating a vector field into such a model [5, 13, 15]. In a preliminary scheme, we simply define $\mathbf{P} = \nabla D + \nabla D'$. Incorporating the curvature-dependent motion and propagation terms, the level set evolution is governed by

$$\frac{\partial u}{\partial t} = \alpha'h(|\nabla I|)|\nabla u|div\frac{\nabla u}{|\nabla u|} + \beta'h(|\nabla I|)|\nabla u| + \gamma'\mathbf{P}\cdot\nabla u,$$
$$(5)$$

where $h$ is a sigmoid function such that $h : R^+ \rightarrow (0, 1]$, $h(0) = 1$, $h(r) \rightarrow 0$ as $r \rightarrow \infty$, and $\alpha'$, $\beta'$ and $\gamma'$ are the scaling parameters.

Note that the initialization is performed by combining $D$ and $D'$. The term $(\gamma'\mathbf{P} \cdot \nabla u)$ in Eq. 5 provides reinforcement towards the boundary calculated from the markers and balance against the mean curvature deformation $\frac{\partial u}{\partial t} = h(|\nabla I(x)|)|\nabla u|div\frac{\nabla u}{|\nabla u|}$. Similar to the parametric model, constant propagation is sometimes necessary. As noted above, an advantage of our approach is that the second term on the right hand side may be replaced by

$$\beta'sgn(M)h(|\nabla I|)|\nabla u|.$$

We believe that this will make it automatically adaptive to the need for either inward or outward propagation. This will remove a practical restriction in the application of the GAC level set model, which is that in practice the model needs to be completely interior or exterior to the true object boundary[13].

# 5 Implementation and Computation

## 5.1 Selecting the desired range of the gradient magnitude

In order for the target boundary to correspond to the gradients that will be located by the balance of the GTDs between the markers, the appropriate band of the gradient magnitude needs to be selectively enhanced. This is a crucial step in using the proposed approach, unless a significant number of markers are used (in $n$D with $n > 1$) and the placement of the markers can be carefully controlled, as otherwise inappropriate selection may result in incorrect gradients being identified and a consequent segmentation failure. The gradient map is transformed as follows:

$$w = \begin{cases} H_w, & |\nabla I| \leq L_i \\ H_w - \frac{|\nabla I| - L_i}{H_i - L_i}(H_w - L_w), & L_i < |\nabla I| < H_i \\ L_w, & |\nabla I| \geq H_i \end{cases} , \quad (6)$$

where the range between $L_i$ and $H_i$ designates the desired gradient magnitude band (we have always chosen $L_i = 0$), $H_w$ is a positive number large enough to ensure a near zero GTD on any topographically flat path between two points in the image, and $L_w$ is a small positive number.

## 5.2 Accurate and Efficient Computation of GTDs

A key component of the proposed method is the computation of the GTDs. Recent advances in applied mathematics have allowed the GTDs to be computed more accurately and efficiently. The GTD function $\tau(x)$, as a special case of the weighted distance transform, satisfies the Eikonal PDE [6] $|\nabla \tau| = \frac{1}{q}$, where $q$ is the speed.

For the speed function, one can use

$$q = \frac{1}{\lambda |\nabla I| + \epsilon}, \quad (7)$$

where $\lambda$ and $\epsilon$ are mapping parameters, and $\epsilon \approx +0$. In practice, we have used the function $w$ in Eq. 6 as an approximation. Thus, the GTDs can be computed using the efficient Fast Marching Method (FMM) [6, 10] developed by Sethian and his associates(e.g. [15]). Compared with alternatives such as those based on chamfer metrics or graph search, FMM both leads to isotropic distance propagation [6], and results in an accuracy that is not limited by the discretization of the image [15]. In fact, FMM yields a solution that is close to the ideal [6]. The maximum difference map (Eq. 2) is efficiently implemented via multiple-front Fast Marching propagation. Only one round of propagation is necessary. For GAC level sets, $D$ and $D'$ are combined to initialize the model in our experiments. In addition, an infinite impulsional response filter that approximates a convolution with the derivative of a Gaussian kernel is used for efficient computation of gradient maps.

# 6 Experiments

Experiments have been conducted using synthetic data, CT and MR data. We present some quantitative evaluations as well as well as preliminary quantitative validations.

## 6.1 Quantitative Evaluations

**Experiments with the Parametric Model**  Two single-voxel markers were employed, one placed randomly in the liver to identify it as the target, the other outside to designate the background. When the background marker was appropriately placed (explained below), the model was able to find and segment the target despite the abundant irrelevant gradients between the initial model and the target (Fig. 2), due to the globally consistent vector field providing guidance in place of image gradients. Our tests have revealed no restriction on the placement of the target marker, other than that it must be interior to the boundary profile of the target structure. On the other hand, these tests also indicate that a background marker will make a useful contribution only if it is not completely encircled by an equally strong or stronger edge than the target's boundary (such as the vertebra). Based on tests conducted so far, examples of where "useful" background markers can be placed for the segmentation of the liver in the image are indicated by the white dots in the lower image of Fig. 2. One possibility to ensure the appropriate placement of a background marker is via intensity and neighborhood tests.

**Experiments with the Geometric Deformable Model**  The integrated 3D GAC level set model has been tested in the segmentation of the lung (on 10 3D images), the brain tumour (on 10 cases) and the knee (6 cases). Within each group of experiments, the same set of parameters have always been applied to all the images used in the group. Satisfactory results have been achieved in each case upon visual inspection. Single-voxel markers were used in the dual-marking approach, one being placed randomly in the target and the other outside. Some examples are shown in (Fig. 3).

## 6.2 Quantitative Studies

**Accuracy**  We used MR images for the quantitative validation of our algorithm. The data used are from the SPL and NSG Brain Tumor Segmentation Database [4], which contains 10 T1-weighted SPGR MR images of the brain[2] together with "ground truth" data. We studied the segmentation of the brain together with the tumours. This is a challenging task as some of the tumours have strong gradients

---

[2] The dimensions of the 10 images are 256 x 256 x 124, with a voxel resolution of 0.9375 x 0.9375 x 1.5 $mm^3$
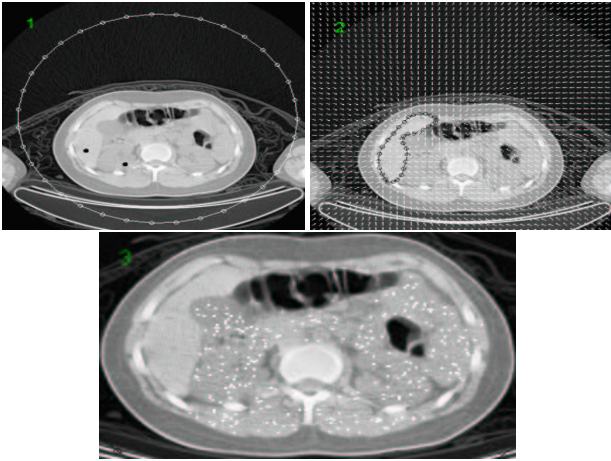
**Figure 2.** *Experiments with a parametric deformable model on a CT image. Upper Left: the image, the initial model (large white circle) and the two markers (black dots) that are use to respectively identify the target and non-target background. Upper Right: the globally consistent vector field (white arrows) and the resultant segmentation (black contour). Lower: Examples showing where a potential background marker should be placed in order for it to make a useful contribution to the segmentation of the Liver. That is, it can be put in any one of the places indicated by the white dots.*



**Figure 3.** *Experiments using a GAC level set model. We used MR brain images and CT lung images. Left column: slice views, with the segmentation superimposed as the transparent overlay. Right column: 3D views of the segmentation result.*

standard deviations (the error bars) resulting from the comparisons are presented, where the left-hand-side bar corresponds to $\frac{False\ Target}{True\ Target}$ and the right $\frac{Missed\ Target}{True\ Target}$.
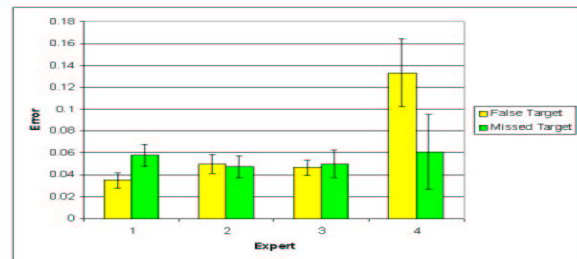


**Figure 4.** *The means (main bars) and standard deviations (error bars) of the differences to the experts' segmentations of the brain on 10 cases.*

at their boundaries. Manual segmentation by four independent human experts was available on a randomly selected 2D slice in each of the ten cases in the SPL and NSG Brain Segmentation Database [4]. For this battery of tests, the "single making" method was used. Typically two markers[3] each comprising of a single voxel were placed with the brain to identify it as the target. No background markers were used. A $\sigma$ value of 1 was used for the smoothing, $H_i = 5.0$, and $\eta = 1500$. We refer to the voxels in the "ground truth" segmentation (the expert's segmentation) as the True Target. We separately consider the False Target (the number of voxels segmented by our method but not by the expert) and the Missed Target (the number of voxels segmented by the expert but not by our method). In Figure 4, the mean errors (the main bars) and the corresponding

**Robustness** Since the maximum difference operation (Eq. 2) that we use means that a single "useful" background marker is sufficient to achieve the desired outcome, we expected the likelihood of success to increase quickly with the number of markers used, even if no tests are performed regarding their placements. To verify this, we used the first 3D image from the SPL and NSG Brain Tumor Segmentation Database, with the target still being a tumor. In Figure 5, we show the failure rates against the number background seeds. These seeds were accepted by a background mask after being randomly generated. The apparent anomaly when 3, 4 and 5 seeds were used can be explained by the fact that between different trials markers were generated independently.

---

[3]In order to overcome the additional challenge of segmenting the normal tissues and the tumours together, however, an additional marker was used in cases where the pathology gives rise to a strong edge, in order to indicate that the pathology was in fact part of the target to be segmented. A further exception is case 9, for which a total of 15 markers were placed inside and around the tumour in order to overcome the strong gradients present in and around the tumour. In this case the tumour and the normal tissues are very difficult to be segmented together using the same parameters applied to the other cases. In all the cases except this one, our trials have indicated that the outcome was insensitive to the placement of the markers. In fact, we failed to observe any effect of the different placements of the markers on the results.
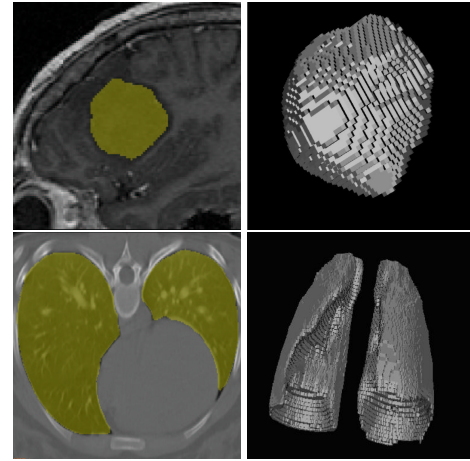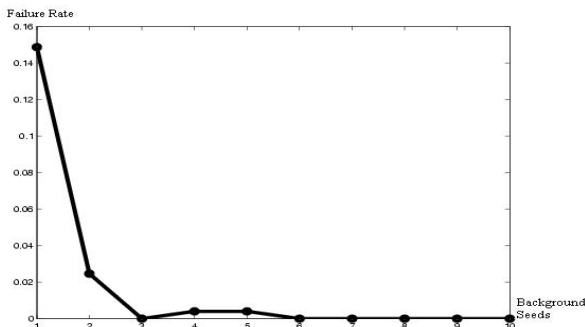
**Figure 5.** *Failure Rate (Y Axis) Vs the Number of Background Seeds Used (X Axis).*

## 7  Conclusions

We have presented the first stage work of a world-first attempt at establishing accurate pediatric computational models for radiation dosimetry. This is a novel approach to reducing the sensitivity to initialization for deformable models using marker-induced vector fields. In this approach, geodesic topographic distances in the gradient image are computed in order to locate the most prominent gradients either between two groups of identifying markers, or surrounding the target marker. This information is integrated into a parametric or geometric deformable model to guide its evolution. Our work takes advantage of theoretical analyses of the watershed transform, yet it is outside of the watershed framework and preserves fully the advantages of deformable models. An accurate and efficient numerical method has been used in the implementation.

Our preliminary experiments have demonstrated that, using this approach, the requirement for (or sensitivity to) the initial input is minimal for both the parametric and the geometric models when a relatively high degree of accuracy needs to be achieved. The main limitation currently is a relative sensitivity to one of the mapping parameters, $H_i$ in Eq. 6. Despite this, we believe that this approach will satisfy the need for a high degree of automation in using deformable models for our dosimetry work, particularly when the seeds can be placed automatically based on anatomical knowledge.

## References

[1] V. Caselles, R. Kimmel, and G. Sapiro. Geodesic active contours. *International Journal of Computer Vision*, 22(1):61–79, 1997.

[2] L. Cohen and I. Cohen. Finite-Element Methods for Active Contour Models and Balloons for 2-D and 3-D Images. *IEEE Transactions on Pattern Analysis and Machine Intelligence*, 15(11):1131–1147, November 1993.

[3] M. Kass, M. Witkin, and D. Terzopoulos. Snakes: active contour models. *International Journal of Computer Vision*, 1:321–331, 1987.

[4] M. Kaus, S. K. Warfield, A. Nabavi, F. A. J. P. M. Black, and R. Kikinis. Automated segmentation of mri of brain tumors. *Radiology*, 218(2):586–591, 2001.

[5] L. M. Lorigo, O. D. Faugeras, W. E. L. Grimson, R. Keriven, R. Kikinis, and C.-F. Westin. Co-dimension 2 geodesic active contours for mra segmentation. In *Int'l Conf. Information Processing in Medical Imaging (IPMI'99)*, pages 126–133, June 28 - July 2 1999.

[6] P. Maragoes, M. A. Butt, and L. F. C. Pessoa. Two frontiers in morphological image analysis: Differential evolution models and hybrid morphological/linear neural networks. In *Proceedings of International Symposium on Computer Graphics, Image processing and Vision*, volume 11, pages 10–17, 1998.

[7] P. Maragos and M. A. Butt. Advances in differential morphology: Image segmentation via eikonal PDE and curve evolution and reconstruction via constrained dilation flow. In H. J. Heijmans and J. B. Roerdink, editors, *Mathematical Morphology and its Applications to Image and Signal Processing*, pages 167–174. Kluwer Academic, Amsterdam, The Netherlands, June 1998.

[8] F. Meyer. Topographic distance and watershed lines. *Signal Processing*, 38:113–125, 1994.

[9] F. Meyer. An overview of morphological segmentation. *International Journal of Pattern Recognition and Artificial Intelligence*, 15(7):1089–1118, 2001.

[10] F. Meyer and P. Maragos. Multiscale morphological segmentations based on watershed, flooding, and eikonal PDE. In M. Nielsen, P. Johansen, O. Olsen, and J. Weickert, editors, *Scale-Space Theories in Computer Vision*, pages 351–362. Springer-Verlag, 1999.

[11] L. Najman and M. Schmitt. Watershed of a continuous function. *Signal Processing*, 38:99–112, July 1994.

[12] H. T. Nguyen, M. I. Worring, and R. van den Boomgaard. Watersnakes: energy-driven watershed segmentation. *IEEE Transactions on Pattern Analysis and Machine Intelligence*, 25(3):330–342, mar 2003.

[13] N. Paragios, O. Mellina-Gottardo, and V. Ramesh. Gradient vector flow fast geometric active contours. *IEEE Transactions on Pattern Analysis and Machine Intelligence*, 26(3):402–417, 2004.

[14] J. B. T. M. Roerdink and A. Meijster. The watershed transform: definitions, algorithms and parallelization strategies. *Fundamenta Informaticae*, 41(1-2):187–228, 2001.

[15] J. Sethian. *Level set methods and fast marching methods: Evolving interfaces in geometry, fluid mechanics, computer vision, and materials science.* Cambridge University Press, 1999.

[16] C. Xu and J. Prince. Snakes, Shapes, and Gradient Vector Flow. *IEEE Transactions on Images Processing*, 7(3):359–369, 1998.